

# Ion and Electron Acoustic Bursts during Anti-Parallel Reconnection Driven by Lasers

Shu Zhang,<sup>1,✉</sup> Abraham Chien,<sup>1</sup> Lan Gao,<sup>2</sup> Hantao Ji,<sup>1,2,✉</sup> Eric G. Blackman,<sup>3</sup> Russ Follett,<sup>4</sup> Dustin H. Froula,<sup>4</sup> Joseph Katz,<sup>4</sup> Chikang Li,<sup>5</sup> Andrew Birkel,<sup>5</sup> Richard Petrasso,<sup>5</sup> John Moody,<sup>6</sup> and Hui Chen<sup>6</sup>

<sup>1</sup>*Department of Astrophysical Sciences, Princeton University, Princeton, New Jersey 08544, USA*

<sup>2</sup>*Princeton Plasma Physics Laboratory, Princeton University, Princeton, New Jersey 08543, USA*

<sup>3</sup>*Department of Physics and Astronomy, University of Rochester, Rochester, New York 14627, USA*

<sup>4</sup>*Laboratory for Laser Energetics, University of Rochester, Rochester, New York 14623, USA*

<sup>5</sup>*Plasma Science and Fusion Center, Massachusetts Institute of Technology, Cambridge, Massachusetts 02139, USA*

<sup>6</sup>*Lawrence Livermore National Laboratory, Livermore, California 94550, USA*

(Dated: September 27, 2022)

Magnetic reconnection is ubiquitous in space and astrophysical plasmas, rapidly converting magnetic field energy into thermal and kinetic energy of plasma particles. Among numerous candidate kinetic mechanisms, ion acoustic instabilities driven by the relative drift between ions and electrons, or electric current, have long been hypothesized to play a critical role in dissipating magnetic energy in collisionless plasmas. But their effectiveness and even existence during reconnection remain elusive due to ion Landau damping and difficulties in resolving the Debye length scale in the laboratory. Here we report a sudden onset of ion acoustic bursts measured by collective Thomson scattering in the exhaust of anti-parallel magnetically driven reconnection in high-Z plasmas at low beta in a novel platform using high-power lasers. The ion acoustic bursts are followed by electron acoustic bursts with electron heating and bulk acceleration. These observations are successfully reproduced by 1D and 2D Particle-in-Cell simulations in which ion acoustic instabilities, driven by electron jet currents in the reconnection exhaust, grow rapidly to form electrostatic double layers. These double layers induce an electron two-stream instability that generates electron acoustic bursts, during which electrons are heated and accelerated in accordance with the experimental measurements. Our results demonstrate the importance of ion and electron acoustic dynamics during magnetic reconnection when ion Landau damping is ineffective, a condition applicable to a range of astrophysical plasmas including near-Earth space, stellar flares, and black hole accretion engines.

Magnetic reconnection is a fundamental physical process through which energy is rapidly converted from magnetic field to plasma by alternating magnetic topology [1, 2]. It has been a longstanding challenge to identify the underlying kinetic mechanisms for efficient dissipation required for the topological change as well as energy conversion to explain the observed fast reconnection in nearly collisionless plasmas in space and astrophysics. There has been progress in understanding and confirming 2D kinetic mechanisms often represented by nongyrotropic pressure tensor [3–6] in the electron diffusion regions (EDRs) where field lines break and reconnect. Beyond these 2D laminar processes, however, the kinetic dissipation mechanisms operating in general 3D are still much less understood [7, 8] within or near diffusion regions and separatrices [9] that feature strong spatial gradients and streaming. They include various plasma waves or instabilities, such as whistler waves [10, 11], Buneman instabilities [12–14], lower-hybrid drift waves (LHDW) [15–22] (due to cross-field gradient [23] or cross-field drift [24]), drift kink [25] or kinetic Kelvin-Helmholtz [26] instabilities.

Among these 3D candidate dissipation mechanisms, unstable ion-acoustic waves (IAWs) [27–30] driven by relative drift between electrons and ions, or equivalently electric current, have attracted considerable interest as potential sources for the enhanced resistivity or viscosity that is often used within fluid descriptions as a lo-

cal, current-dependent anomalous resistivity required for the sustained Petschek model of fast reconnection [31–36]. Despite early pioneering laboratory detection [37], however, the importance of IAWs for magnetic reconnection has been quickly dismissed due to the widely observed high ion temperature ( $T_i/Z \gtrsim T_e$ ) in space and in the laboratory where IAWs are strongly stabilized by ion Landau damping. Technical difficulties in the laboratory in measuring plasma waves in the short wavelengths on the order of Debye length have also prevented progress on identifying IAWs and understanding their detailed properties and role in magnetic reconnection.

In this Article, we present a novel laboratory platform where reconnection is driven magnetically at low- $\beta$  by laser-powered capacitor coils [38] in high-Z plasmas where  $T_i/Z \ll T_e$ . Sudden onset of bursts of IAWs is successfully measured for the first time in the exhaust region by collective Thomson scattering diagnostics. The IAWs are followed by bursts of electron acoustic waves (EAWs) with electron heating and bulk acceleration. The corresponding Particle-in-Cell (PIC) simulations in 1D and 2D show that IAWs are destabilized by electron exhaust jet where relative drift between ions and electrons is large. IAWs grow rapidly to form electrostatic double layers which in turn accelerate electrons to drive two-stream instability generating bursts of EAWs while heating electrons. Our results demonstrate the importance of ion and electron acoustic dynamics causing bursty energy

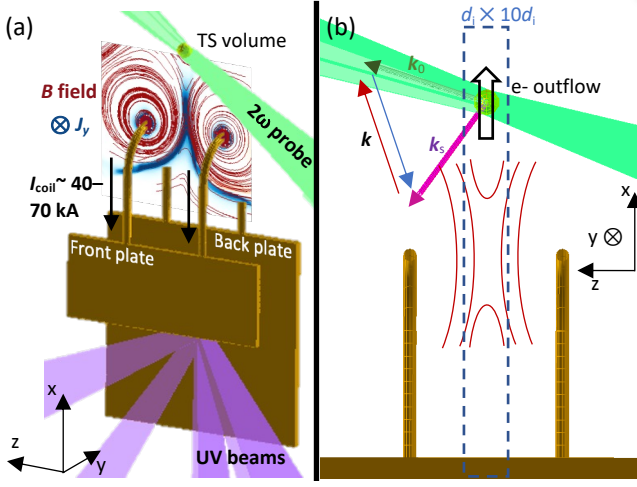


FIG. 1. Experimental setup. Six UV beams are used to irradiate the back plate of the capacitor, driving current in the coils with  $I_{\text{coil}} \sim 40 - 70$  kA. FLASH MHD simulation results are overlapped in (a) to show the structure of the magnetic field (red lines) and the out-of-plane current density (blue) in the  $y$ -direction. A  $2\omega$  (527 nm) Thomson scattering beam (green) probes the reconnection exhaust region,  $600 \mu\text{m}$  above the center point between the top of the coils. The scattered light in a volume  $60 \times 60 \times 50 \mu\text{m}^3$  is collected by an  $f/10$  reflective collection system.  $\mathbf{k}_0$  and  $\mathbf{k}_s$  in (b) are the wavevectors of the probe beam and the collected scattered light. The red and blue arrows indicate wavevectors ( $\mathbf{k}$ ) of waves in plasma resonant with the probe and the scattered light. The red arrow is for the wave generating redshifted scattered light, and the blue arrow is for the wave generating blueshifted scattered light. These  $\mathbf{k}$ 's are in the  $x - y$  plane and  $17^\circ$  off the outflow direction. The blue dashed box indicates a  $d_i \times 10d_i = 180 \mu\text{m} \times 1800 \mu\text{m}$  region, in which  $d_i = c/\omega_{pi}$ .

dissipation during magnetic reconnection when ion Landau damping is ineffective. Implications for reconnection process in magnetically dominated plasmas during stellar flares and accretion onto black holes are discussed.

### RECONNECTION PLATFORM WITH LASER-DRIVEN CAPACITOR COILS

The presented experiments were performed on the OMEGA laser facility at the Laboratory for Laser Energetics, University of Rochester [39]. The experimental platform is shown in Fig. 1. The capacitor-coil target is made of a  $50 \mu\text{m}$  thick Cu foil. Two wires connecting front and back plates are bent to  $600 \mu\text{m}$  diameter half-circle coils and  $500\text{-}\mu\text{m}$  straight legs and are separated by  $600 \mu\text{m}$ . The target pictures are presented in supplemental Fig. S4. Six beams of  $500 \text{ J}$   $1\text{-ns}$  UV ( $\lambda = 351 \text{ nm}$ ) lasers are focused on the center of the capacitor's back plate to drive a  $\sim 40 - 70$  kA current in the coils forming an anti-parallel magnetic field. The laser-generated plasmas diffuse into the region between the coils, and

the x-rays and the current also heat the coils generating plasmas. The plasma between the coils is magnetized by the coil-driven antiparallel magnetic field forming a reconnection current sheet.

The magnetic field generated by the capacitor-coil targets is measured using proton radiography [40–42]. The upstream magnetic field strength is  $\sim 23 - 40 \text{ T}$  at  $6 \text{ ns}$  after the lasers' onset. The proton radiographs also show the reconnection current sheet exists, and the data and analyses are discussed in Supplementary. To further quantify the reconnection conditions, we have conducted radiative and non-ideal magnetohydrodynamic (rad-MHD) simulations using the FLASH code [43] to simulate the plasma diffusing from the capacitor plates and the plasma emerging from the heated coils due to Ohmic heating and x-ray radiation. The supplemental materials detail the setup of the non-ideal rad-MHD simulation. The simulated magnetic field lines and the current density at  $3 \text{ ns}$ , overlapped on the target in Fig. 1(a), show that a reconnection current sheet is formed between the coils. This reconnection current sheet lasts until  $10 \text{ ns}$ , as shown in supplemental Fig. S2. The synthetic proton radiographs shown in supplemental Fig. S3 have a current sheet-induced central flask-like feature, consistent with the experimental one.

A unique approach to studying kinetic instabilities in reconnection is provided by combining a laser-driven capacitor-coil reconnection platform with collective Thomson scattering. Collective Thomson scattering diagnoses the spectrum of the density fluctuations in plasmas, which may be the microturbulence induced by kinetic instabilities [44–46]. It can also diagnose the Stokes and anti-Stokes scattering of natural resonances in plasmas, such as ion-acoustic waves (IAW) and electron plasma waves (EPW). Since the plasma parameters determine the spectrum of the IAWs and EPWs-induced scattering, Thomson scattering is frequently used to diagnose the plasma's densities, temperatures, mean ion charge, flow speed, and electron-ion relative drift as well as non-Maxwellian distributions [47–53].

In this experiment, we recorded the Thomson scattering spectrogram of a probe laser ( $\lambda = 527 \text{ nm}$ ,  $150 \text{ J}$  energy,  $3.7 \text{ ns}$  square pulse,  $60 \mu\text{m}$  spot size) focused at  $600 \mu\text{m}$  ( $\sim 3d_i$ ) above the center between the top of the coils as shown in Fig. 1. As shown in Fig. 1(b), the directions of the probe light and the scattered light collector determine the wavevector  $\mathbf{k}$  of the measured density fluctuations or natural resonances since  $\mathbf{k} = \mathbf{k}_0 - \mathbf{k}_s$  or  $\mathbf{k} = \mathbf{k}_s - \mathbf{k}_0$ .  $\mathbf{k}$  is in the direction  $17^\circ$  from the outflow direction ( $+\mathbf{x}$ ) and  $k \sim k_0 = 2\pi/527 \text{ nm}^{-1}$ . To infer the exhaust plasma's parameters, we fit the synthetic Thomson scattering spectra to the measured spectra. The synthetic spectrum is calculated based on Eq. (2) in the Method section. The least-square fit suggests that the plasma in the exhaust region has electron density  $n_e \sim 5 \times 10^{18} \text{ cm}^{-3}$ , electron temperature

$T_e \sim 200 - 300$  eV, mean ion charge  $Z \sim 18$  and flow velocity  $v \sim 1.5 - 3.5 \times 10^5$  m/s, which roughly matches the Alfvén speed ( $1.2 - 2.0 \times 10^5$  m/s).

### BURSTS OF ION AND ELECTRON ACOUSTIC WAVES AND ELECTRON HEATING

The Thomson scattering from the ion-acoustic waves (IAW) reveals that current-driven instabilities develop at 7 ns. The narrowband spectrometer captured the asymmetric (10:1) IAW Stokes and anti-Stokes peaks. The scattering signals grow from thermal level by three orders of magnitude to extremely intense, bursty and asymmetric ( $\sim 100:1$ ) IAW peaks during 7-8 ns. This is shown in Fig. 2(a), as a sign of the ion turbulence induced by unstable IAW [46]. The asymmetry in the IAW Stokes and anti-Stokes peaks is the feature of the drift between electrons and ions inducing different Landau damping rates for IAWs in different directions [54]. As shown in Fig. 2(c), the Thomson scattering spectrum lineout before the IAW bursts (along the dashed line in Fig. 2a) can be reproduced in the synthetic spectrum (green dashed line in Fig. 2c) when electrons ( $n_e = 5 \times 10^{18} \text{ cm}^{-3}$ ,  $T_e = 200$  eV) are drifting with  $v_d = 0.17\sqrt{T_e/m_e}$  relative to ions ( $T_i = 400$  eV,  $Z = 18$ ). The IAW-resonant peak is broader than the synthetic spectrum (green dashed line) which assumes flow velocity is uniform in the scattering volume, but the broader peak can be reproduced by including inhomogeneity of the flow velocity with  $\Delta v = 2 \times 10^4$  m/s, which may be induced by turbulence or a spatial gradient of the flow velocity. The synthetic spectrum calculation assumes the resonant wave is stable or the density fluctuations are at the thermal level. However, based on the electrostatic dispersion equation,

$$1 - \frac{\omega_{pe}^2}{2k^2 T_e/m_e} Z' \left( \frac{\omega/k - v_d}{\sqrt{2T_e/m_e}} \right) - \frac{\omega_{pi}^2}{2k^2 T_i/m_i} Z' \left( \frac{\omega/k}{\sqrt{2T_i/m_i}} \right) = 0, \quad (1)$$

where  $Z'$  is the derivative of the plasma dispersion function [55], the plasma with this strong electron drift is unstable to IAW, and the maximum growth rate is  $17 \text{ ns}^{-1}$  ( $1.4 \times 10^{-4} \omega_{pe}$ , and 0.058 ns e-folding time) at  $k = 0.33/\lambda_{De}$  ( $\lambda_{De} = \sqrt{T_e/m_e}/\omega_{pe}$ ). The wavelength is 6 times longer than the electron's mean-free-path, which suggests that the collisions for electrons are negligible for the IAW growth. This IAW growth agrees with the exponential growth of the scattering signal, which is proportional to the square of the density fluctuation. As shown in Fig. 3(b), before the first spike, the TS IAW signal exponentially grows with an 0.025 ns e-folding time, about 40% of the calculated IAW growth rate. The intensity of the IAW scattering is 3 orders higher than that when

no burst presents near 5 ns, indicating that the fluctuation amplitude ( $\delta n/n$  at  $k = 2\pi/527 \text{ nm}^{-1}$ ) is  $\sim 30$  times higher than the thermal level.

With about 0.12 ns delay from the bursts of the IAW (see Fig. 3(c)), the EAW appears with spectra red-shifted by  $\sim 13$  nm wavelength, corresponding to a phase velocity of  $0.025c \sim 1.2\sqrt{T_e/m_e}$ . This EAW peak can be reproduced with a two-stream distribution shown in Fig. 2(d). The red solid line in the inserted figure is the two-stream distribution that produces the synthetic spectrum with a strong EAW peak (red solid line). The velocity at the valley of the distribution matches the phase velocity of the EAW peak.

The amplitude of IAW and EAW during the bursty period (7-8 ns) is shown to be modulated at a frequency of  $\sim 7$  GHz (Fig. 3d), close to the lower-hybrid frequency ( $\sqrt{f_{ce}f_{ci}}$ ) at  $B = 20$  T. One candidate to explain such observations is the Modified Two-Stream Instability (MTSI) [24] driven by the electron outflow jet perpendicular to the local magnetic field in the exhaust region. The MTSI can generate electric field fluctuations nearly parallel to the current, which may modulate the IAW and the generation of EAW bursts. Waves near the lower-hybrid frequency were often observed in the MMS (Magnetospheric Multi-Scale) mission [e.g. 56] and the MRX (Magnetic Reconnection Experiment) [e.g. 16] and have been suggested to mediate energy dissipation. This modulation near the lower-hybrid frequency suggests instabilities like MTSI may affect the electron outflow, but further study is needed to characterize the role of this lower-hybrid modulation.

Electron heating is also captured since electron temperature increases by 60% during the bursts of IAW and EAW. Electron temperature is measured from the separation between the IAW's Stokes and anti-Stokes peaks, which is proportional to the ion-acoustic velocity as  $\Delta\omega \sim 2k\sqrt{ZT_e/m_i}$ . This IAW peak separation increases by 25% before (7.0 ns) and after (8.5 ns) the IAW and EAW bursts.

### 1D LOCAL PARTICLE-IN-CELL SIMULATION

To understand the bursts of the correlated IAW and EAW, we have used a 1D electrostatic particle-in-cell code [57] to simulate the thermal electrons (initial electron temperature  $T_{e0} = 320$  eV) drifting relative to ions with a velocity  $v_d = 0.5\sqrt{T_{e0}/m_e}$ .

The bursts of IAW and EAW are reproduced in the 1D PIC simulation, as shown in Fig. 4. The dispersion plot Fig. 4(b) shows that the EAW burst has a phase velocity of  $\sim 1.3\sqrt{T_{e0}/m_e}$  with a broadband frequency of  $\sim (0.1 - 1) \omega_{pe}$ . This phase velocity roughly agrees with the experimentally observed EAW's phase velocity  $\sim 1.2\sqrt{T_e/m_e}$ . In the phase space shown in Fig. 4(d), this EAW corresponds to the phase space holes

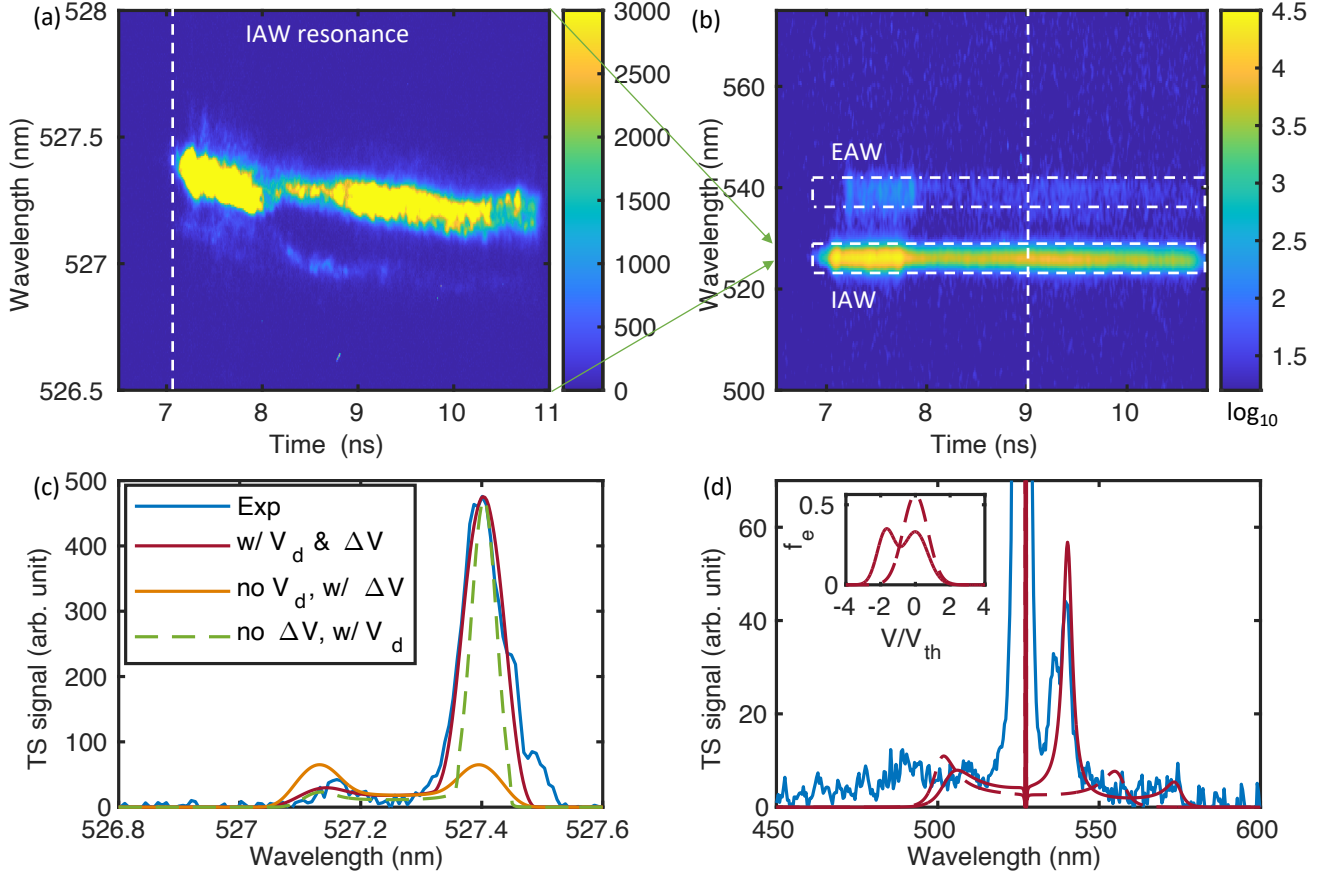


FIG. 2. (a) (b) Time-resolved Thomson scattering (TS) at  $t = 7 - 10$  ns. The IAW resonant peaks in (a) are highly asymmetric (grow from 10:1 to 100:1). The spectrum at 7.1 ns, before the IAW bursts, along the vertical dashed line in (a) is plotted in (c) as the blue line and compared with the synthetic TS spectra. The green dashed synthetic spectrum in (c) can reproduce the asymmetry of the IAW peaks, which is calculated with electrons streaming relative to ions with  $v_d = 0.17v_{th}$  along the  $k$ -direction (red arrow) in Fig. 1b. In addition to the electron drift, an inhomogeneous flow velocity with  $\Delta v = 2 \times 10^4$  m/s  $\sim v_i$  in the scattering volume can broaden the IAW peak, shown as the red solid line, to match the experiment. A plasma without a drift but with an inhomogeneous flow velocity would generate a symmetric IAW spectrum, shown as the orange line. (b) is the spectrogram from the broadband spectrometer showing both the EAW resonance and the IAW feature. The spectrum at 9 ns (along the vertical dashed line of (b)) is plotted in (d) with a fitted synthetic spectrum (red solid line). A two-stream electron distribution, shown as the solid line in the inserted plot, is needed to reproduce the strong EAW signal.  $-v$  direction is along the redshifted  $k$  in Fig. 1b. The velocity at the valley of the distribution ( $-0.023c$ ) matches the EAW's phase velocity ( $0.025c$ ). For reference, a Maxwellian distribution, shown as the dashed line in the inserted figure, would generate the dashed spectrum.

which originated from the electron-two-stream instability downstream of a double layer generated by the unstable IAW. This double layer reflects low-energy electrons and accelerates high-energy electrons that can overcome the potential well, resulting in a two-stream distribution. This process has been discovered in Vlasov simulations [58], which also shows that, with a realistic mass ratio, the double layer occurs  $\sim 10^4 \omega_{pe}^{-1}$  after the peak of the IAW fluctuations, which is consistent with the observed  $0.12$  ns  $\sim 1.5 \times 10^4 \omega_{pe}^{-1}$  delay between the EAW and IAW bursts.

## 2D GLOBAL PARTICLE-IN-CELL SIMULATION

In addition to the 1D local PIC simulation showing the unstable IAW-generated double layer and EAWs, our 2D PIC reconnection simulation also confirms the double layer generation in the outflow region when cold background plasma is present. In the 2D reconnection simulation with cold background plasma, double layers in the outflow are developed and create non-Maxwellian and broadened distributions in the double layer downstream. Figure 5(a) is the in-plane current map and magnetic field lines in the entire simulation domain. The ion density profile in the outflow region is shown in Fig. 5(b), in which the double layers are presented as the ion cavities

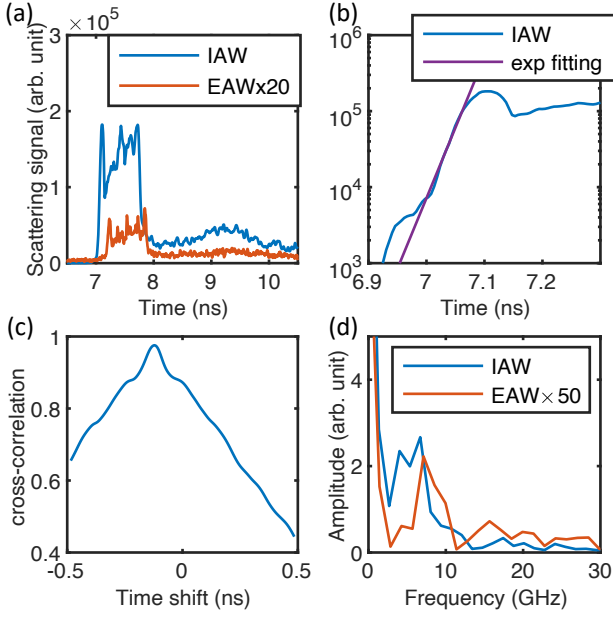


FIG. 3. (a) IAW and EAW Thomson scattering signal in the dash-boxed (IAW) and dash-dot-boxed (EAW) region shown in Fig. 2(b). Bursts of IAW and EAW are shown around 7 – 8 ns. (b) is the zoomed-in plot of (a) in log scale to show the growth phase of the IAW signal, which is fitted by an exponential function with e-folding time 0.025 ns ( $3200 \omega_{pe}^{-1}$ ), agreeing with the IAW growth rate,  $\gamma \sim 1.4 \times 10^{-4} \omega_{pe}$ . (c) Cross-correlation of the IAW and EAW signal shows a strong correlation between IAW and EAW. IAW is leading EAW by 0.12 ns  $\sim 1.5 \times 10^4 \omega_{pe}^{-1}$ . (d) The Fourier transform of the 7–8 ns signal shows that both IAW and EAW signals are oscillating with an amplitude peak frequency at 7 GHz. This frequency matches the lower-hybrid frequency in a 20 T magnetic field.

cycled in red. The electron phase space profile crossing the double layers at  $z = -74d_e$  is plotted in Fig. 5(c). As shown in the phase space profile, upstream of the double layers, the electrons are drifting relative to ions, which can destabilize IAW forming double layers. In the downstream, the distribution is broadened and shows a non-Maxwellian distribution with double peaks. Besides the current-driven unstable IAW, ion-ion acoustic instability [59] is also shown in the region with two-streaming ions ( $x \sim 500d_e$  in Fig. 5b), especially in the 100 and 400 mass ratio cases. However, this ion-ion acoustic instability only creates strong density perturbations; no non-Maxwellian distribution is seen in electron phase space. Meanwhile, the double layers and the downstream non-Maxwellian distribution are persistent with different mass ratios. The observation of the current-driven double layers and the induced non-Maxwellian distribution confirm that, with cold background plasmas, the current-driven IAW bursts can result in energy dissipation in the outflow region.

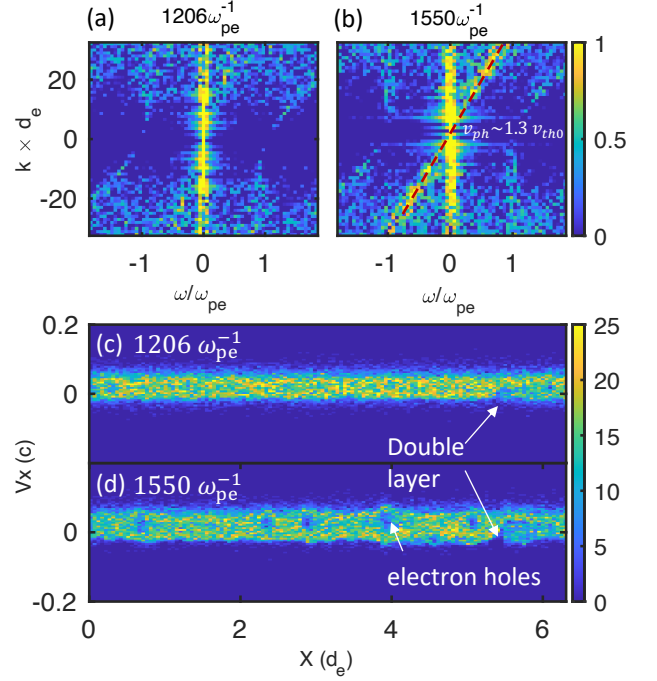


FIG. 4. (a) and (b) Electron density dispersion plots before ( $t = 1206 \omega_{pe}^{-1}$ ) and during the EAW bursts ( $t = 1550 \omega_{pe}^{-1}$ ). Wavenumber  $k$  is normalized by  $1/d_e$  ( $d_e = c/\omega_{pe}$ ). The red dashed line is the dispersion relation with  $v_{ph} = 1.3 \sqrt{T_e/m_e}$ . (c) and (d) are the electron phase spaces at the times of (a) and (b) respectively. (c) shows the double layer starts to form at  $t = 1206 \omega_{pe}^{-1}$ . (d) After forming the double layer at  $t = 1550 \omega_{pe}^{-1}$ , the electron holes are generated due to the two-stream instabilities downstream of the double layer. These electron holes are moving in the  $+x$  direction with a velocity of  $1.3 \sqrt{T_e/m_e}$ , forming the EAW bursts shown in (b).

## DISCUSSION AND OUTLOOK

In summary, our low- $\beta$  magnetic reconnection experiments using laser-driven capacitor coils exhibit current-driven IAW bursts, followed by EAW bursts with electron heating in the exhaust region.

The location and wave direction are consistent with the IAWs observed by MMS [60], THEMIS (Time History of Events and Macroscale Interactions during Substorms) [61], and PSP (Parker Solar Probe) [62] when a population of cold ions exists in the background and their Landau damping is ineffective. These observations suggest that the current-driven instabilities can lead to a bursty magnetic field energy release. As our 1D and 2D PIC simulations reveal, this energy dissipation process involves IAW-formed double layers producing two-streaming electrons downstream, which induces the electron two-stream instability. This rapidly heats the electrons, braking the electron outflow jet. Such a double-layer-induced electron two-stream instability may also explain the origin of the EAWs observed by MMS [63].

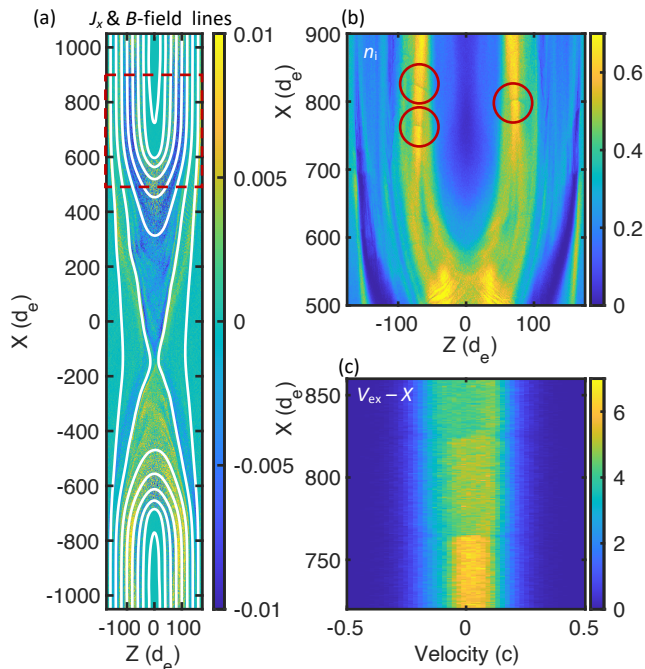


FIG. 5. Results of the 2D reconnection PIC simulation with  $m_i/m_e = 1600$  at  $104000 \omega_{pe}^{-1}$ . (a) The entire profile of the background electron current in  $x$ -direction ( $J_x = en_{e,bg}v_x$  normalized to  $en_0c$ ) with magnetic field lines. (b) A cropped region of the background plasma's ion density in the outflow region (red dashes in a). The double layers, shown as the ion cavities, are cycled in red. (c) Electron phase space profile along  $z = -74d_e$  crossing the double layers at  $x = 765$  and  $825 d_e$ .

This dissipation process in the reconnection exhaust region is confirmed in our experiment; whether this process can occur in the current sheet region needs further study. A similar mechanism has been observed in the current sheet of a 3D PIC simulation with a strong guide field, in which Buneman instability [12] leads to a formation of double layers and triggers electron two-stream instability [14]. In 1D simulations, the Buneman-instability-generated double layer also creates ion and electron phase space holes [64, 65]. However, without a guide field or with a weak guide field, the electrons would be deflected out of the current sheet within a short period, which is shown in 3D simulations with a finite guide field [66]. The non-steady electron stream in the current sheet may interrupt the instabilities' growth. The growth of IAW and double layer needs  $\sim 10^3 - 10^4 \omega_{pe}^{-1}$ , as suggested by our experiment. In addition to the time needed, Vlasov simulation and previous particle simulations [67] all demonstrate that generating the double layer requires a large system size ( $> 500\lambda_{De}$ ). Future experiments and large-scale 3D simulations are needed to study the current sheet region.

The IAW-type turbulence may be important for stellar flares and other plasmas where magnetic reconnection is

prevalent, including those of black hole accretion engines. During the initial transient phase of stellar flares, for example, electrons are heated to high temperatures, and ions could remain cold and evade detection [68]. This condition favors destabilizing IAWs to dissipate current and thus magnetic free energy via electrostatic double layers, in turn triggering EAW and further heating electrons. Type-III and type-U radio emission [69] could be generated by electron beams out of double layer structures.

Other low electron  $\beta$  two-temperature plasmas, in which the electrons may be much cooler than ions, may exist in strongly magnetized black hole accretion disk corona [70] or regions within collisionless accretion flows [71, 72]. Here, the relative drift between electrons and ions can be sufficiently large compared with the electron thermal speed to overcome ion Landau damping due to simultaneous low density and low electron temperature (or equivalently electron  $\beta \ll 1$ ), and thus unstable IAW or the related Buneman instabilities may be viable mechanisms to efficiently dissipate magnetic energy.

In this context, we note that the observed current-driven unstable IAW provides a collisionless coupling of ions and electrons: during the current-driven unstable IAW, the magnetic energy is converted to the ion energy in IAW and eventually forms the double layer that provides an electric potential. The double layer stores both ion kinetic energy and electric potential energy, which is then transferred to electron kinetic energy by accelerating electrons that pass through the double layer potential well, and heating electrons by the two-stream instability. In standard two-temperature accretion models used to explain curiously quiescent accretors, the rate of coupling between ions and electrons is assumed to be purely Coulomb collisional coupling, or parameterized [71, 72] freely. In these models, the accretion produces low luminosity when the ions acquiring free energy from viscosity are unable to transfer their energy to radiating electrons on an accretion time scale. Whether a collisionless faster-than-Coulomb coupling exists in these contexts has been a long-standing open question because the answer can dramatically affect the paradigm as to why these sources appear so quiescent. As such, it will be important to quantify how the specific mechanism that we have identified scales to the astrophysical contexts in future work.

We would like to thank Dr. Qing Wang, Dr. Lee Suttle, Dr. Jack Halliday, Dr. Sergey Lebedev and Dr. William Daughton for fruitful discussions. We acknowledge the OMEGA laser facility staff at the Laboratory for Laser Energetics. The research presented is supported by the DOE Office of Science under the HEDLP program with award number DE-SC0020103. The experiment was conducted at the Omega Laser Facility with the beam time through the National Laser Users' Facility (NLUF) under the auspices of the U.S. DOE/NNSA by the University of Rochester's Laboratory for Laser Energetics

under Contract DE-NA0003856. C.K.L., A.B. and R.P. are supported under the auspices of the U.S. DOE/NNSA under Contract DE-NA0003868. The FLASH code used in this work was in part developed by the DOE NNSA-ASC OASCR Flash Center at the University of Chicago. The authors would like to acknowledge the OSIRIS Consortium, consisting of UCLA and IST (Lisbon, Portugal) for providing access to the OSIRIS 4.0 framework supported by NSF ACI-1339893.

This report was prepared as an account of work sponsored by an agency of the U.S. Government. Neither the U.S. Government nor any agency thereof, nor any of their employees, makes any warranty, express or implied, or assumes any legal liability or responsibility for the accuracy, completeness, or usefulness of any information, apparatus, product, or process disclosed, or represents that its use would not infringe privately owned rights. Reference herein to any specific commercial product, process, or service by trade name, trademark, manufacturer, or otherwise does not necessarily constitute or imply its endorsement, recommendation, or favoring by the U.S. Government or any agency thereof. The views and opinions of authors expressed herein do not necessarily state or reflect those of the U.S. Government or any agency thereof.

## METHODS

In the methods section, we present the setup of the Thomson scattering diagnostics, the calculation of the synthetic Thomson scattering spectrum, and the parameters of the 1D and 2D PIC simulations. The FLASH radiative-non-ideal magnetohydrodynamic simulations and the proton radiography used to confirm the existence of reconnection are presented in the supplemental material.

### Collective Thomson scattering

In this experiment, a  $f/10$  reflective collection system  $63^\circ$  off the probe's axis [73] collects the scattered light from a  $60 \times 60 \times 50 \mu\text{m}^3$  volume near the focus. A narrowband (7 nm window) and a broadband (320 nm window) streaked spectrometers temporally and spectrally resolved the collected scattering light. The streak window is 5 ns. The narrowband spectrometer covers the light scattered by ion-acoustic waves. The broadband spectrometer can show the spectrum of the light scattered by EAW, EPW, and the merged IAW peaks. The timing of the probe is changed for each shot to cover the entire reconnection process.

To forward fit the measured Thomson scattering spectrum, we calculated the synthetic power spectrum in Fig. 2 and Fig. 6 based on the model summarized in

Ref. [47]. The synthetic power spectrum for arbitrary velocity distributions is

$$P(\lambda_s) \propto \left(1 + \frac{2\omega}{\omega_0}\right) \left[ \frac{2\pi}{k} \left| \frac{1 + \chi_i}{1 + \chi_e + \chi_i} \right|^2 f_e\left(\frac{\omega}{k}\right) + \frac{2\pi Z}{k} \left| \frac{\chi_e}{1 + \chi_e + \chi_i} \right|^2 f_i\left(\frac{\omega}{k}\right) \right] \frac{d\omega}{d\lambda_s}, \quad (2)$$

where  $\omega = \omega_s - \omega_0$  is the angular frequency of the fluctuations scattering the probe light ( $\omega_0, \mathbf{k}_0$ ) and generating the scattered light ( $\omega_s, \mathbf{k}_s$ ), and  $f_{e,i}(v)$  are the electron/ion velocity distributions reduced to 1D along  $\mathbf{k}$  direction. The electron and ion susceptibilities are given by

$$\chi_{e,i}(\omega, k) = \int_{-\infty}^{\infty} dv \frac{\omega_{pe,i}^2}{k^2} \frac{k \partial f_{e,i} / \partial v}{\omega - kv}. \quad (3)$$

### Electron acoustic wave resonance in Thomson scattering

Figure 6(a) shows the time evolution of the Thomson scattering spectrum from the broadband spectrometer, and the spectrum at 2.9 ns is shown as the blue line in Fig. 6(b). In addition to the Stokes and anti-Stokes scattering of the EPW usually seen in thermal plasmas, the Thomson scattering spectrum also shows resonant peaks with lower wavelength shift ( $\sim 10$  nm) indicating the non-Maxwellian distribution in the reconnection exhaust. These shorter wavelength resonant peaks are caused by EAWs with phase velocities near the electron thermal velocity  $v_{e,th} = \sqrt{T_e/m_e}$ , which would be Landau damped if the electron velocity distribution was Maxwellian, as shown in the red dashed line in Fig. 6(b). To reproduce the EAW peaks, we modified the distribution function by combining two counter-streaming beams with the steady component to reduce the slope near the thermal speed shown as the solid red line in Fig. 6(c). The solid line in Fig. 6(b) shows the fitted scattering spectrum calculated based on Eq. (2). This three-component distribution is similar to the observed ring-core distribution in reconnection PIC simulations [74], in which the ring in the outflow-out-of-plane phase space ( $v_x - v_y$ ) reduces to two counter-streaming beams in  $v_x$ . This ring structure is likely produced by the reconnected magnetic field ( $B_y$ ) turning the accelerated electrons [75]. Similar ring-core distribution has also been observed by MMS in the reconnection exhaust region [5, 6].

### 1D PIC simulation

The simulation was performed in a  $2\pi c/\omega_{pe}$  ( $2\pi d_e$ ) periodic domain with a reduced ion mass  $m_i/m_e = 100$  and

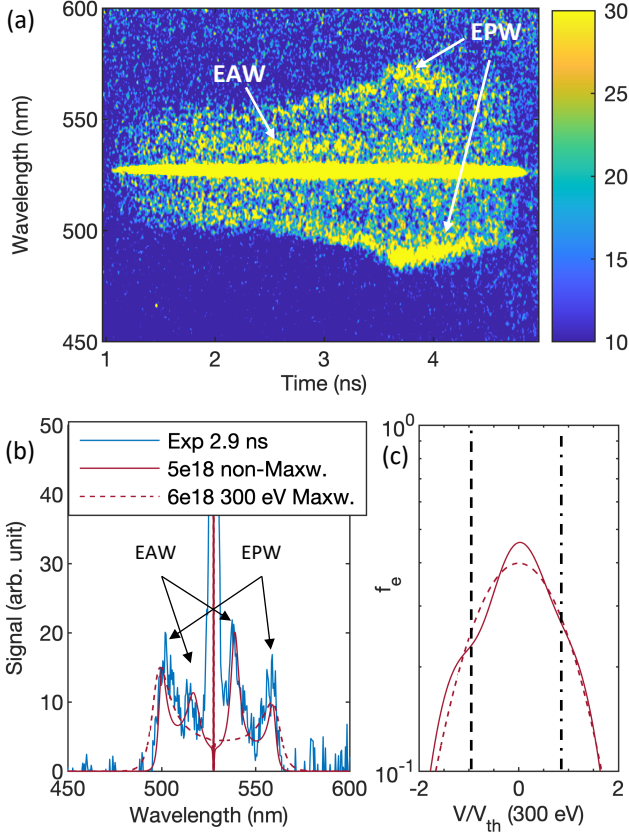


FIG. 6. (a) Time-resolved Thomson scattering (TS) shows features of electron plasma waves (EPW) and electron acoustic waves (EAW). The UV lasers onset at 0 ns. (b) Comparison between the measured TS spectrum at  $t = 2.9$  ns and the synthetic TS spectra with Maxwellian electrons ( $T_e = 300$  eV, dashed) vs. non-Maxwellian electrons (solid). The velocity distribution functions are plotted in (c). The non-Maxwellian distribution (solid line in c) is constructed with two secondary components ( $n_e = 1.15 \times 10^{18} \text{ cm}^{-3}$ ,  $T_e = 75$  eV) streaming with  $-1.2v_{th,300\text{eV}}$  and  $+1.1v_{th,300\text{eV}}$  relative to a steady electron component ( $n_e = 2.7 \times 10^{18} \text{ cm}^{-3}$ ,  $T_e = 75$  eV).  $-v$  direction is along the redshifted  $\mathbf{k}$  in Fig. 1b. This non-Maxwellian distribution reduced the slope near the phase velocities of the EAWs, marked with a dashed line corresponding to the EAW at 539 nm and a dash-dotted line for the EAW at 517 nm. The non-Maxwellian component is required to match the data.

a lower ion temperature  $T_i = 20$  eV to keep the ion thermal speed lower than the IAW's phase velocity. The simulation domain contains 256 cells and 128 particles per cell. To mimic the induction electric field that would arise from the dissipation of the bipolar magnetic field, we have added an external electric field  $E_x = 10^{-5}m_e c \omega_{pe}/e$  to the electric field calculated by the Poisson equation for advancing the particles' velocity.

## 2D PIC simulation

The 2D PIC simulations use OSIRIS code [76, 77] to simulate a Harris current sheet [78] and a cold background plasma initialized with a density profile as

$$n_{bg}(z) = 0.3n_0 \left[ \frac{1}{2} + \frac{1}{2} \tanh \left( \frac{|z| - 2L}{0.5L} \right) \right], \quad (4)$$

where  $n_0$  is the peak density of the Harris current sheet and  $L = 20d_e$ . This simulation setup is similar to the cold background simulation described in Ref. [79]. The Harris current sheet has hot ions with  $T_{i,harris} = 5T_{e,harris}$ . The background plasma is initialized with  $T_{i,bg} = T_{e,bg} = T_{e,harris}/25$ . The anti-parallel magnetic field is in  $x$  direction with  $B_x = B_0 \tanh(z/L)$ , where  $B_0/em_e = \omega_{ce} = 0.5\omega_{pe}$ . A long-wavelength perturbation [80] with  $0.01B_0$  amplitude is included to initialize reconnection. The simulation has a  $2100d_e \times 350d_e$  box size in  $6144 \times 1024$  cells. The boundaries are periodic in the  $x$  direction. The  $z$  direction boundaries are reflective for particles and conductive for the electric field. The mass ratio has been scanned with  $m_i/m_e = 100, 400$ , and 1600.

## DATA AVAILABILITY

The experimental Thomson scattering spectrograms are available on request from corresponding authors.

## CODE AVAILABILITY

The synthetic Thomson scattering calculation code is available on request from corresponding authors. The 1D electrostatic PIC simulation code is available in Ref. [57]. The Osiris 4.0 PIC simulation code is available to authorized users signed MoUs with the Osiris Consortium, consisting of IST and UCLA. FLASH rad-MHD code is available from [flash.rochester.edu](http://flash.rochester.edu). The plasma dispersion relation calculation code is available on the PlasmaDispersionRelation repo at <https://github.com/xiaoshulittletree>.

✉ [shuzhang@princeton.edu](mailto:shuzhang@princeton.edu)  
✉ [hji@pppl.gov](mailto:hji@pppl.gov)

- [1] M. Yamada, R. Kulsrud, and H. Ji, *Rev. Mod. Phys.* **82**, 603 (2010).
- [2] H. Ji, W. Daughton, J. Jara-Almonte, A. Le, A. Stanier, and J. Yoo, *Nat. Rev. Phys.* **4** (2022), [10.1038/s42254-021-00419-x](https://doi.org/10.1038/s42254-021-00419-x).
- [3] M. Hesse, K. Schindler, J. Birn, and M. Kuznetsova, *Phys. Plasmas* **6**, 1781 (1999).
- [4] R. Kulsrud, H. Ji, W. Fox, and M. Yamada, *Phys. Plasmas* **12**, 082301 (2005).

- [5] J. L. Burch, R. B. Torbert, T. D. Phan, L.-J. Chen, T. E. Moore, R. E. Ergun, J. P. Eastwood, D. J. Gershman, P. A. Cassak, M. R. Argall, S. Wang, M. Hesse, C. J. Pollock, B. L. Giles, R. Nakamura, B. H. Mauk, S. A. Fuselier, C. T. Russell, R. J. Strangeway, J. F. Drake, M. A. Shay, Y. V. Khotyaintsev, P.-A. Lindqvist, G. Marklund, F. D. Wilder, D. T. Young, K. Torkar, J. Goldstein, J. C. Dorelli, L. A. Avanov, M. Oka, D. N. Baker, A. N. Jaynes, K. A. Goodrich, I. J. Cohen, D. L. Turner, J. F. Fennell, J. B. Blake, J. Clemmons, M. Goldman, D. Newman, S. M. Petriner, K. J. Trattner, B. Lavraud, P. H. Reiff, W. Baumjohann, W. Magnes, M. Steller, W. Lewis, Y. Saito, V. Coffey, and M. Chandler, *Science* **352**, aaf2939 (2016).
- [6] R. B. Torbert, J. L. Burch, T. D. Phan, M. Hesse, M. R. Argall, J. Shuster, R. E. Ergun, L. Alm, R. Nakamura, K. J. Genestreti, D. J. Gershman, W. R. Paterson, D. L. Turner, I. Cohen, B. L. Giles, C. J. Pollock, S. Wang, L.-J. Chen, J. E. Stawarz, J. P. Eastwood, K. J. Hwang, C. Farrugia, I. Dors, H. Vaith, C. Mouikis, A. Ardakani, B. H. Mauk, S. A. Fuselier, C. T. Russell, R. J. Strangeway, T. E. Moore, J. F. Drake, M. A. Shay, Y. V. Khotyaintsev, P.-A. Lindqvist, W. Baumjohann, F. D. Wilder, N. Ahmadi, J. C. Dorelli, L. A. Avanov, M. Oka, D. N. Baker, J. F. Fennell, J. B. Blake, A. N. Jaynes, O. Le Contel, S. M. Petriner, B. Lavraud, and Y. Saito, *Science* **362**, 1391 (2018).
- [7] H. Ji, Y. Ren, M. Yamada, S. Dorfman, W. Daughton, and S. P. Gerhardt, *Geophys. Res. Lett.* **35**, L13106 (2008).
- [8] G. Cozzani, Y. V. Khotyaintsev, D. B. Graham, J. Egedal, M. André, A. Vaivads, A. Alexandrova, O. Le Contel, R. Nakamura, S. A. Fuselier, C. T. Russell, and J. L. Burch, *Phys. Rev. Lett.* **127**, 215101 (2021), [arXiv:2103.12527 \[physics.plasm-ph\]](https://arxiv.org/abs/2103.12527).
- [9] G. Lapenta, S. Markidis, A. Divin, D. Newman, and M. Goldman, *Journal of Plasma Physics* **81**, 325810109 (2015).
- [10] C. Kennel and H. Petschek, *J. Geophys. Res.* **71**, 1 (1966).
- [11] M. V. Goldman, D. L. Newman, G. Lapenta, L. Andersson, J. T. Gosling, S. Eriksson, S. Markidis, J. P. Eastwood, and R. Ergun, *Phys. Rev. Lett.* **112**, 145002 (2014).
- [12] O. Buneman, *Phys. Rev. Lett.* **1**, 8 (1958).
- [13] J. Drake, M. Swisdak, C. Cattell, M. Shay, B. Rogers, and A. Zeiler, *Science* **299**, 873 (2003).
- [14] H. Che, J. F. Drake, M. Swisdak, and P. H. Yoon, *Phys. Rev. Lett.* **102**, 145004 (2009).
- [15] T. Carter, H. Ji, F. Trintchouk, M. Yamada, and R. Kulsrud, *Phys. Rev. Lett.* **88**, 015001 (2002).
- [16] H. Ji, S. Terry, M. Yamada, R. Kulsrud, A. Kuritsyn, and Y. Ren, *Phys. Rev. Lett.* **92**, 115001 (2004).
- [17] H. Ji, R. Kulsrud, W. Fox, and M. Yamada, *J. Geophys. Res.* **110**, A08212 (2005).
- [18] W. Fox, M. Porkolab, J. Egedal, N. Katz, and A. Le, *Phys. Plasmas* **17**, 072303 (2010).
- [19] J. Yoo, J. Jara-Almonte, E. Yerber, S. Wang, T. Qian, A. Le, H. Ji, M. Yamada, W. Fox, E.-H. Kim, *et al.*, *Geophysical Research Letters* **45**, 8054 (2018).
- [20] D. B. Graham, Y. V. Khotyaintsev, C. Norgren, A. Vaivads, M. André, J. Drake, J. Egedal, M. Zhou, O. Le Contel, J. Webster, *et al.*, *Journal of Geophysical Research: Space Physics* **124**, 8727 (2019).
- [21] L.-J. Chen, S. Wang, O. Le Contel, A. Rager, M. Hesse, J. Drake, J. Dorelli, J. Ng, N. Bessho, D. Graham, L. B. Wilson, T. Moore, B. Giles, W. Paterson, B. Lavraud, K. Genestreti, R. Nakamura, Y. V. Khotyaintsev, R. E. Ergun, R. B. Torbert, J. Burch, C. Pollock, C. T. Russell, P.-A. Lindqvist, and L. Avanov, *Phys. Rev. Lett.* **125**, 025103 (2020).
- [22] J. Yoo, J.-Y. Ji, M. V. Ambat, S. Wang, H. Ji, J. Lo, B. Li, Y. Ren, J. Jara-Almonte, L.-J. Chen, *et al.*, *Geophysical Research Letters* **47**, e2020GL087192 (2020).
- [23] N. Krall and P. Liewer, *Phys. Rev. A* **4**, 2094 (1971).
- [24] J. McBride, E. Ott, J. Boris, and J. Orens, *Phys. Fluids* **15**, 2367 (1972).
- [25] W. Daughton, *J. Geophys. Res.* **104**, 28701 (1999).
- [26] T. Nakamura, H. Hasegawa, W. Daughton, S. Eriksson, W. Y. Li, and R. Nakamura, *Nature communications* **8**, 1 (2017).
- [27] B. Coppi and A. B. Friedland, *The Astrophysical Journal* **169**, 379 (1971).
- [28] D. F. Smith and E. Priest, *The Astrophysical Journal* **176**, 487 (1972).
- [29] F. Coroniti and A. Evitar, *Ap. J. Suppl. Series* **33**, 89 (1977).
- [30] R. Z. Sagdeev, *Rev. Mod. Phys.* **51**, 1 (1979).
- [31] M. Ugai and T. Tsuda, *J. Plasma Phys.* **17**, 337 (1977).
- [32] T. Sato and T. Hayashi, *Phys. Fluids* **22**, 1189 (1979).
- [33] J. Aparicio, M. G. Haines, R. J. Hastie, and J. P. Wainwright, *Physics of Plasmas* **5**, 3180 (1998), <https://doi.org/10.1063/1.873046>.
- [34] R. Kulsrud, *Phys. Plasmas* **5**, 1599 (1998).
- [35] R. Kulsrud, *Earth Planets Space* **53**, 417 (2001).
- [36] D. A. Uzdensky, *Astrophys. J.* **587**, 450 (2003).
- [37] W. Gekelman and R. Stenzel, *Journal of Geophysical Research: Space Physics* **89**, 2715 (1984).
- [38] A. Chien, L. Gao, S. Zhang, H. Ji, E. G. Blackman, W. Daughton, A. Stanier, A. Le, F. Guo, R. Follett, H. Chen, G. Fiksel, G. Bleotu, R. C. Cauble, S. N. Chen, A. Fazzini, K. Flippo, O. French, D. H. Froula, J. Fuchs, S. Fujioka, K. Hill, S. Klein, C. Kuranz, P. Nilson, A. Rasmus, and R. Takizawa, “Direct measurement of non-thermal electron acceleration from magnetically driven reconnection in a laboratory plasma,” (2022), [arXiv:2201.10052 \[physics.plasm-ph\]](https://arxiv.org/abs/2201.10052).
- [39] T. Boehly, D. Brown, R. Craxton, R. Keck, J. Knauer, J. Kelly, T. Kessler, S. Kumpan, S. Loucks, S. Letzring, F. Marshall, R. McCrory, S. Morse, W. Seka, J. Soures, and C. Verdon, *Optics Communications* **133**, 495 (1997).
- [40] L. Gao, H. Ji, G. Fiksel, W. Fox, M. Evans, and N. Alfonso, *Physics of Plasmas* **23**, 043106 (2016), <https://doi.org/10.1063/1.4945643>.
- [41] A. Chien, L. Gao, H. Ji, X. Yuan, E. G. Blackman, H. Chen, P. C. Efthimion, G. Fiksel, D. H. Froula, K. W. Hill, K. Huang, Q. Lu, J. D. Moody, and P. M. Nilson, *Physics of Plasmas* **26**, 062113 (2019), <https://doi.org/10.1063/1.5095960>.
- [42] A. Chien, L. Gao, S. Zhang, H. Ji, E. Blackman, H. Chen, G. Fiksel, K. Hill, and P. Nilson, *Physics of Plasmas* **28**, 052105 (2021), <https://doi.org/10.1063/5.0044048>.
- [43] B. Fryxell, K. Olson, P. Ricker, F. X. Timmes, M. Zingale, D. Q. Lamb, P. MacNeice, R. Rosner, J. W. Truran, and H. Tufo, *The Astrophysical Journal Supplement Series* **131**, 273 (2000).
- [44] A. L. Milder, J. Zielinski, J. Katz, W. Rozmus, D. Edgell, A. Hansen, M. Sherlock, C. Bruulsema, J. P. Palastro,

- D. Turnbull, and D. H. Froula, *Phys. Rev. Lett.* **129**, 115002 (2022).
- [45] D. H. Froula, L. Divol, D. G. Braun, B. I. Cohen, G. Gregori, A. Mackinnon, E. A. Williams, S. H. Glenzer, H. A. Baldi, D. S. Montgomery, and R. P. Johnson, *Physics of Plasmas* **10**, 1846 (2003), <https://doi.org/10.1063/1.1542887>.
- [46] C. C. Daughney, L. S. Holmes, and J. W. M. Paul, *Physical Review Letters* **25**, 497 (1970).
- [47] D. H. Froula, S. H. Glenzer, N. C. J. Luhmann, and J. Sheffield, *Plasma scattering of electromagnetic radiation: theory and measurement techniques; 2nd ed.* (Elsevier, Amsterdam, 2011).
- [48] L. G. Suttle, J. D. Hare, S. V. Lebedev, G. F. Swadling, G. C. Burdiak, A. Ciardi, J. P. Chittenden, N. F. Loureiro, N. Niasse, F. Suzuki-Vidal, J. Wu, Q. Yang, T. Clayson, A. Frank, T. S. Robinson, R. A. Smith, and N. Stuart, *Phys. Rev. Lett.* **116**, 225001 (2016).
- [49] J. D. Hare, L. Suttle, S. V. Lebedev, N. F. Loureiro, A. Ciardi, G. C. Burdiak, J. P. Chittenden, T. Clayson, C. Garcia, N. Niasse, T. Robinson, R. A. Smith, N. Stuart, F. Suzuki-Vidal, G. F. Swadling, J. Ma, J. Wu, and Q. Yang, *Phys. Rev. Lett.* **118** (2017).
- [50] L. G. Suttle, J. D. Hare, J. W. D. Halliday, S. Merlini, D. R. Russell, E. R. Tubman, V. Valenzuela-Villaseca, W. Rozmus, C. Bruulsema, and S. V. Lebedev, *Review of Scientific Instruments* **92**, 033542 (2021), <https://doi.org/10.1063/5.0041118>.
- [51] K. Sakai, S. Isayama, N. Bolouki, M. S. Habibi, Y. L. Liu, Y. H. Hsieh, H. H. Chu, J. Wang, S. H. Chen, T. Morita, K. Tomita, R. Yamazaki, Y. Sakawa, S. Matsukiyo, and Y. Kuramitsu, *Physics of Plasmas* **27**, 103104 (2020), <https://doi.org/10.1063/5.0011935>.
- [52] G. F. Swadling, C. Bruulsema, F. Fiuza, D. P. Higginson, C. M. Huntington, H.-S. Park, B. B. Pollock, W. Rozmus, H. G. Rinderknecht, J. Katz, A. Birkel, and J. S. Ross, *Phys. Rev. Lett.* **124**, 215001 (2020).
- [53] A. L. Milder, H. P. Le, M. Sherlock, P. Franke, J. Katz, S. T. Ivancic, J. L. Shaw, J. P. Palastro, A. M. Hansen, I. A. Begishev, W. Rozmus, and D. H. Froula, *Physical Review Letters* **124**, 025001 (2020).
- [54] J. Hawreliak, D. M. Chambers, S. H. Glenzer, A. Gouveia, R. J. Kingham, R. S. Marjoribanks, P. A. Pinto, O. Renner, P. Soundhauss, S. Topping, E. Wolfrum, P. E. Young, and J. S. Wark, *Journal of Physics B: Atomic, Molecular and Optical Physics* **37**, 1541 (2004).
- [55] B. D. Fried and S. D. Conte, *The plasma dispersion function: the Hilbert transform of the Gaussian* (Academic Press, 1961).
- [56] Y. V. Khotyaintsev, D. B. Graham, K. Steinvall, L. Alm, A. Vaivads, A. Johlander, C. Norgren, W. Li, A. Divin, H. S. Fu, K.-J. Hwang, J. L. Burch, N. Ahmadi, O. Le Contel, D. J. Gershman, C. T. Russell, and R. B. Torbert, *Phys. Rev. Lett.* **124**, 045101 (2020).
- [57] G. Lapenta, “Particle in cell methods with application to simulations in space weather,”.
- [58] A. R. Vazsonyi, K. Hara, and I. D. Boyd, *Physics of Plasmas* **27**, 112303 (2020), <https://doi.org/10.1063/5.0019729>.
- [59] S. P. Gary and N. Omid, *Journal of Plasma Physics* **37**, 45–61 (1987).
- [60] K. Steinvall, Y. V. Khotyaintsev, D. B. Graham, A. Vaivads, M. André, and C. T. Russell, *Geophysical Research Letters* **48**, e2020GL090286 (2021).
- [61] H. Uchino, S. Kurita, Y. Harada, S. Machida, and V. Angelopoulos, *Journal of Geophysical Research: Space Physics* **122**, 3291 (2017).
- [62] F. S. Mozer, C. A. Cattell, J. Halekas, I. Y. Vasko, J. L. Verniero, and P. J. Kellogg, “Core electron heating by triggered ion acoustic waves in the solar wind,” (2021), [arXiv:2111.07161](https://arxiv.org/abs/2111.07161) [astro-ph.SR].
- [63] R. E. Ergun, J. C. Holmes, K. A. Goodrich, F. D. Wilder, J. E. Stawarz, S. Eriksson, D. L. Newman, S. J. Schwartz, M. V. Goldman, A. P. Sturmer, D. M. Malaspina, M. E. Usanova, R. B. Torbert, M. Argall, P.-A. Lindqvist, Y. Khotyaintsev, J. L. Burch, R. J. Strangeway, C. T. Russell, C. J. Pollock, B. L. Giles, J. J. C. Dorelli, L. Avanov, M. Hesse, L. J. Chen, B. Lavraud, O. Le Contel, A. Retino, T. D. Phan, J. P. Eastwood, M. Oieroset, J. Drake, M. A. Shay, P. A. Cassak, R. Nakamura, M. Zhou, M. Ashour-Abdalla, and M. André, *Geophys. Res. Lett.* **43**, 5626 (2016).
- [64] R. A. Smith, *Physica Scripta* **T2A**, 238 (1982).
- [65] M. V. Goldman, D. L. Newman, and R. E. Ergun, *Non-linear Processes in Geophysics* **10**, 37 (2003).
- [66] W. Daughton, V. Roytershteyn, H. Karimabadi, L. Yin, B. Albright, B. Bergen, and K. Bowers, *Nature Phys.* **7**, 539 (2011).
- [67] T. Sato and H. Okuda, *Phys. Rev. Lett.* **44**, 740 (1980).
- [68] V. Polito, J. Dudík, J. Kašparová, E. Dzifčáková, K. K. Reeves, P. Testa, and B. Chen, *The Astrophysical Journal* **864**, 63 (2018).
- [69] R. Miteva, G. Mann, C. Vocks, and H. Aurass, *Astronomy & Astrophysics* **461**, 1127 (2007).
- [70] T. Di Matteo, E. G. Blackman, and A. C. Fabian, *MNRAS* **291**, L23 (1997), [arXiv:astro-ph/9705079](https://arxiv.org/abs/astro-ph/9705079) [astro-ph].
- [71] R. Narayan, R. Mahadevan, and E. Quataert, in *Theory of Black Hole Accretion Disks*, edited by M. A. Abramowicz, G. Björnsson, and J. E. Pringle (1998) pp. 148–182.
- [72] F. Yuan and R. Narayan, *Ann. Rev. Astron. Astrophys.* **52**, 529 (2014).
- [73] J. Katz, R. Boni, C. Sorce, R. Follett, M. J. Shoup, and D. H. Froula, *Review of Scientific Instruments* **83**, 10E349 (2012), <https://doi.org/10.1063/1.4733551>.
- [74] J. R. Shuster, L.-J. Chen, W. S. Daughton, L. C. Lee, K. H. Lee, N. Bessho, R. B. Torbert, G. Li, and M. R. Argall, *Geophysical Research Letters* **41**, 5389 (2014).
- [75] N. Bessho, L.-J. Chen, J. R. Shuster, and S. Wang, *Geophysical Research Letters* **41**, 8688 (2014).
- [76] R. Fonseca, L. Silva, R. Hemker, F. Tsung, V. Decyk, W. Lu, C. Ren, W. Mori, S. Deng, S. Lee, T. Katsouleas, J. Adam, and Osiris, in *Lect. Notes comput. Sci.* (Springer-Verlag, 2002) p. Vol. 2331.
- [77] R. G. Hemker, “Particle-in-cell modeling of plasma-based accelerators in two and three dimensions,” (2015), [arXiv:1503.00276](https://arxiv.org/abs/1503.00276) [physics.comp-ph].
- [78] E. Harris, *Il Nuovo Cimento* **23**, 115 (1962).
- [79] C. Norgren, P. Tenfjord, M. Hesse, S. Toledo-Redondo, W.-Y. Li, Y. Xu, N. K. Kwagala, S. Spinnangr, H. Kolstø, and T. Moretto, *Frontiers in Astronomy and Space Sciences* **8**, 149 (2021).
- [80] J. Birn, J. Drake, M. Shay, B. Rogers, R. Denton, M. Hesse, M. Kuznetsova, Z. Ma, A. Bhattacharjee, A. Otto, and P. Pritchett, *J. Geophys. Res.* **106**, 3715 (2001).